analytical chemistry

pubs.acs.org/ac Article

Microfluidic Ratiometric Photoelectrochemical Biosensor Using a Magnetic Field on a Photochromic Composite Platform: A Proof-of-Concept Study for Magnetic-Photoelectrochemical Bioanalysis

Qian Cheng, Jinhui Feng,* Tingting Wu, Nuo Zhang, Xueying Wang, Hongmin Ma, Xu Sun, and Qin Wei*

Cite This: *Anal. Chem.* 2021, 93, 13680−13686 Read Online

ACCESS | Metrics & More | Article Recommendations | Supporting Information

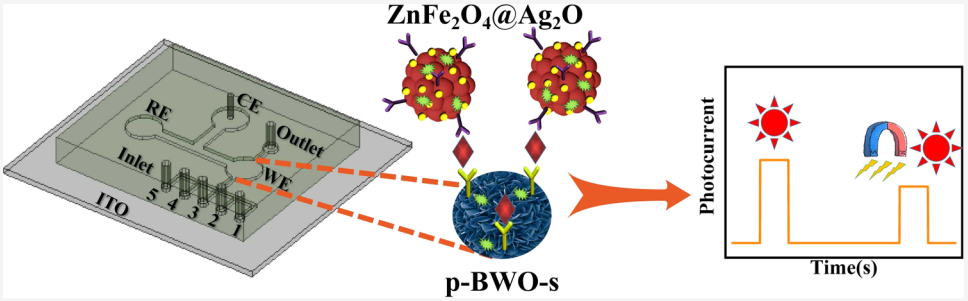

ABSTRACT: Integrating a microfluidic sensor with a ratiometric photoelectrochemical (PEC) strategy to build a bioanalysis device for actual sample testing is often limited to large-volume space-resolution equipment and wavelength-dependent or potential-dependent paired photoactive materials. This work reports a microfluidic ratiometric magnetic-photoelectrochemical (M-PEC) biosensor on the photochromic composite platform to solve the above problems. In particular, as a proof-of-concept study, the platform Bi_2WO_{6-x}/amorphous BiOCl nanosheets/Bi_2S_3 (p-BWO-s) mediated by photochromic color centers and the magnetic photoactive secondary antibody marker $ZnFe_2O_4$@Ag_2O are integrated on the microfluidic biosensor. By enhancement of the photochromic color centers, p-BWO-s outputs a considerable photocurrent signal. Meanwhile, the photoactivity of the secondary antibody marker can be changed with a magnetic field; thus, different photocurrent signals can be obtained to realize ratiometric detection. The quenching photocurrent signal without the magnetic field and the difference photocurrent signal under the magnetic field are quantitatively related to the target concentration, which unfolds a novel general strategy for bioanalysis. Different from traditional ratiometric PEC biosensors, this work characterizes the first ratiometric PEC biosensor based on an external magnetic field. Generally speaking, combined with different biorecognition cases, this scheme with good expansibility brings a unique new perspective.

1. INTRODUCTION

Recently, microfluidic sensors have developed rapidly due to their advantages such as portability, less sample consumption, rapid detection, and easy integration.[1−3] As a subfield of microfluidic sensors, microfluidic photoelectrochemical (PEC) biosensors have attracted much attention due to their low background, high sensitivity, and low cost.[4−6] Although remarkable achievements have been obtained in this field, there are still many opportunities to improve the sensitivity of this technology. The traditional PEC biosensors rely on the electrical signal generated under the action of light. The photocurrent signal is easy to be interfered because of the disturbance of light intensity, the distance between the electrode and the light source, the small change of buffer solution, and other external interference factors. Fortunately, the ratiometric sensing strategy brings the dawn for the effective elimination of interference factors. And it makes an indelible contribution to eliminating false-negative or false-positive signals. At present, there are many outstanding works, such as spatial-resolved,[7] potential-resolved,[8] and wavelength-resolved[9] ratiometric PEC sensing strategies. Although these works have undoubtedly injected a lot of vitality into the development of ratiometric PEC biosensors, the drawback is that these strategies often depend on large-volume space-resolution equipment and wavelength-dependent or potential-dependent paired photoactive materials. In other words, it is

Received: July 27, 2021
Accepted: September 20, 2021
Published: September 29, 2021

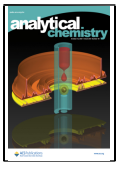

https://doi.org/10.1021/acs.analchem.1c03171
Anal. Chem. 2021, 93, 13680−13686

Scheme 1. (A) Preparation Process of Ab_2-$ZnFe_2O_4$@Ag_2O, (B) Construction Procedure for the Sensing Zone of Microfluidic Ratiometric M-PEC Biosensor, and (C) Testing Process for the Microfluidic Ratiometric M-PEC Biosensor

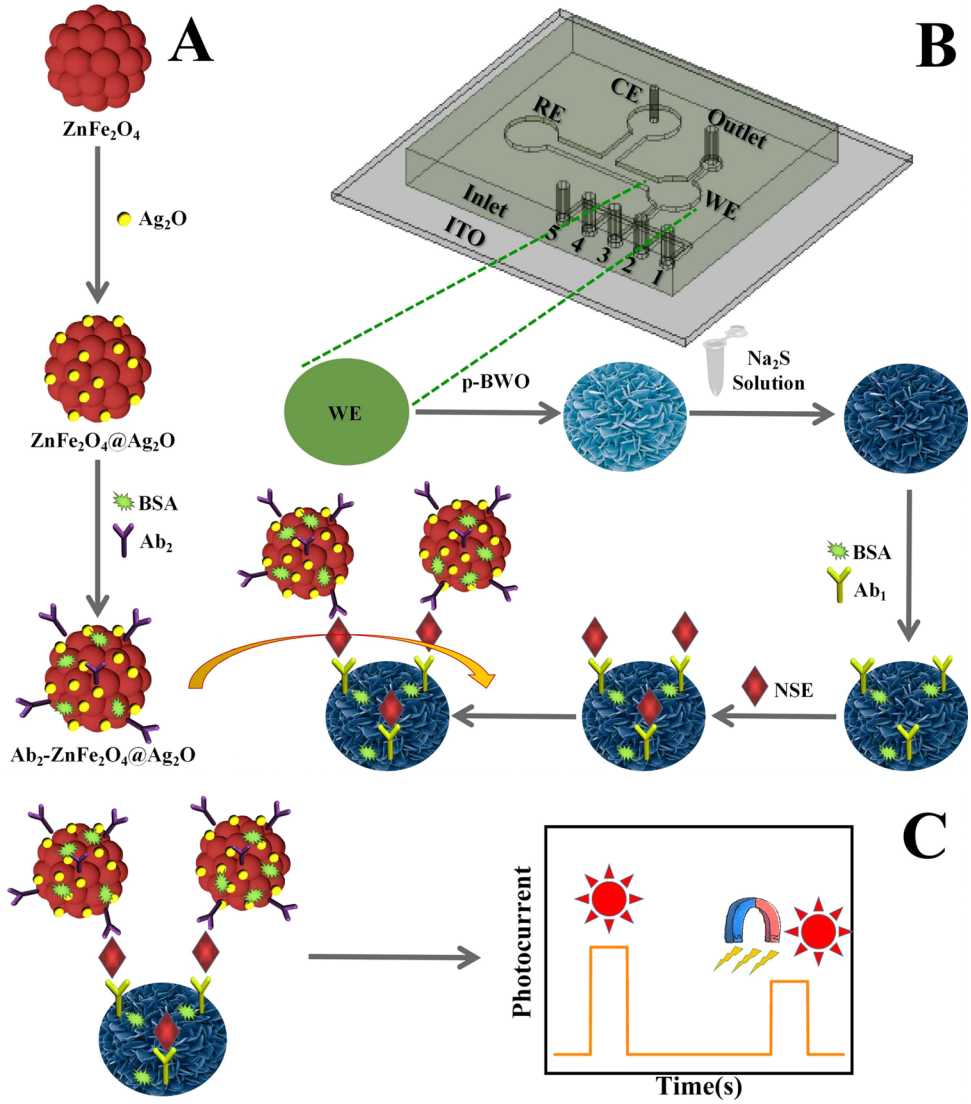

necessary to find a more universal ratiometric PEC sensing strategy.

Herein, we report a concept for a microfluidic ratiometric magnetic-photoelectrochemical (M-PEC) biosensor. In recent years, the influence of the external field on photoactive materials has been widely concerned,[10,11] including temperature gradient,[12−14] magnetic field,[15,16] external electric field,[17,18] microwave,[1920] mechanical stress,[21,22] and coupled external field.[23] The magnetic field, as a typical noncontact external field, can improve the performance of photoactive materials without introducing a complex preparation process and changing the geometry or components of photoactive materials. Under the action of the magnetic field, the properties of magnetic photoactive materials such as the spin state,[24] magnetoresistance,[25] and other states may change. And these changes often produce a positive effect on the separation of photogenerated electron−hole pairs. Inspired by this principle, we hypothesized and verified that the photocurrent signals of the biosensor are different in the absence of a magnetic field and in the presence of a magnetic field due to the effect of the magnetic field on magnetic photoactive secondary antibody markers. Compared with other types of ratiometric PEC biosensors, the M-PEC biosensor is more inclusive to the platform materials or analytes, more universal, and also suitable for miniaturization. As we know, no relevant work has been published on this sensing mode.

Another key point in this work is to choose an innovative photoactive platform. It is widely known that defects are closely related to some important physical and chemical properties of photoactive materials.[26,27] Here, we adopted a method to promote the effective separation of electron−hole pairs in the platform by photochromic color centers. The $W(VI)O_{6-x}$ unit defects with photochromic properties in Bi_2WO_{6-x}/amorphous BiOCl nanosheets (hereinafter referred to as p-BWO) can rapidly capture and deliver the photogenerated electrons through the cyclic transformation of the valence state of W. After in situ vulcanization, the Bi_2S_3-modified p-BWO (hereinafter referred to as p-BWO-s) can realize the rapid separation of electron−hole pairs by the defects, leading to the larger photocurrent signal and higher sensitivity.

Based on the above, the photochromic composite p-BWO-s as a platform material to provide a considerable basal signal, the neuron-specific enolase (NSE) antigen as a representative

https://doi.org/10.1021/acs.analchem.1c03171
Anal. Chem. 2021, 93, 13680−13686

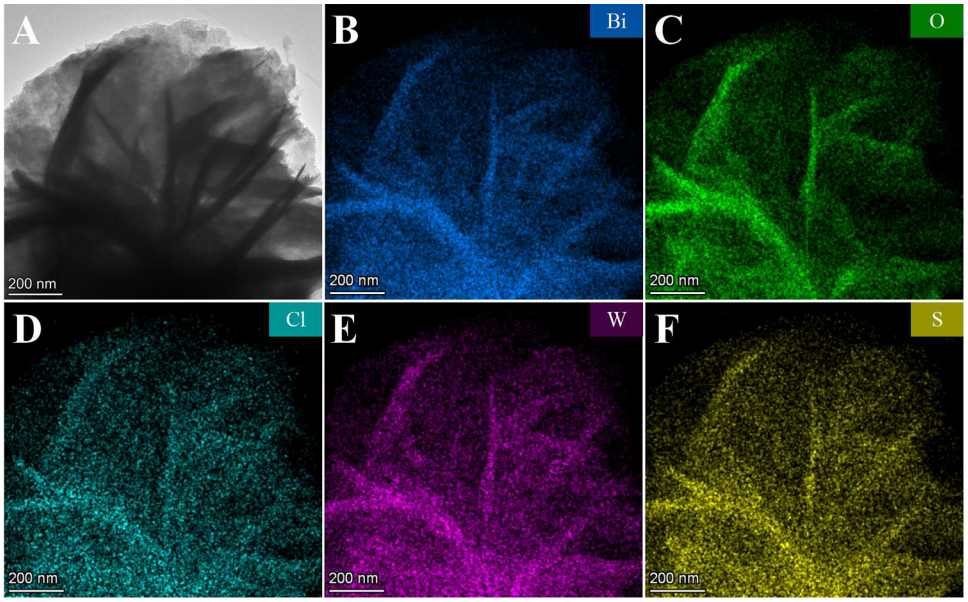

Figure 1. HRTEM image of p-BWO-s composites (A) and elemental mappings of Bi (B), O (C), Cl (D), W (E), and S (F), corresponding to the image of panel (A).

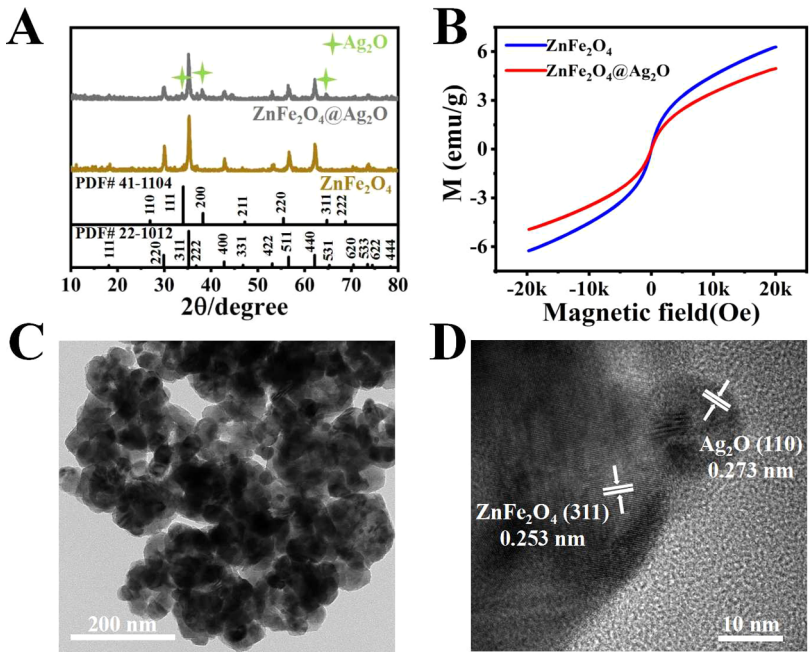

Figure 2. XRD patterns of (A) $ZnFe_2O_4$ and $ZnFe_2O_4$@Ag_2O. Magnetization curves of (B) $ZnFe_2O_4$ and $ZnFe_2O_4$@Ag_2O. HRTEM images of (C, D) $ZnFe_2O_4$@Ag_2O.

recognition target, and the magnetic photoactive $ZnFe_2O_4$@Ag_2O as a secondary antibody marker, a magnetic-resolved microfluidic ratiometric PEC biosensor was constructed as shown in Scheme 1. The photocurrent signal is changed by the effect of the magnetic field on photoactivity of $ZnFe_2O_4$@Ag_2O. And the biosensor also has satisfactory results in repeatability, selectivity, and stability for NSE detection. It is worth noting that as a general concept, this biosensor can be used to detect other biological analytes. It may even be extended to other modes, such as magnetic-electrochemiluminescence biosensors, magnetic-electrochemical biosensors, and so on.

2. EXPERIMENTAL SECTION

Microelectrodes were designed by wet etching and silk-screen printing as shown in Scheme S1. Also, Figure S1 shows the real photo of the microelectrode. And the construction process of the microfluidic ratiometric M-PEC biosensor is shown in Scheme 1. Specifically, 8 μL of chitosan solution (0.5 wt % with 1% acetic acid) (from inlet 1) was injected into the p-BWO-s working electrode (WE) for 30 min. Similarly, 8 μL of glutaraldehyde (0.5 wt %) (from inlet 1) was also injected into the p-BWO-s WE for 30 min. Later, 10 μL of Ab_1 (10 μg/mL) (from inlet 2) was injected for 30 min. After incubation for 60 min at 37 °C, the modified WE was injected into 10 μL of bovine serum albumin (BSA) (0.1 wt %) (from inlet 3) to

https://doi.org/10.1021/acs.analchem.1c03171
Anal. Chem. 2021, 93, 13680−13686

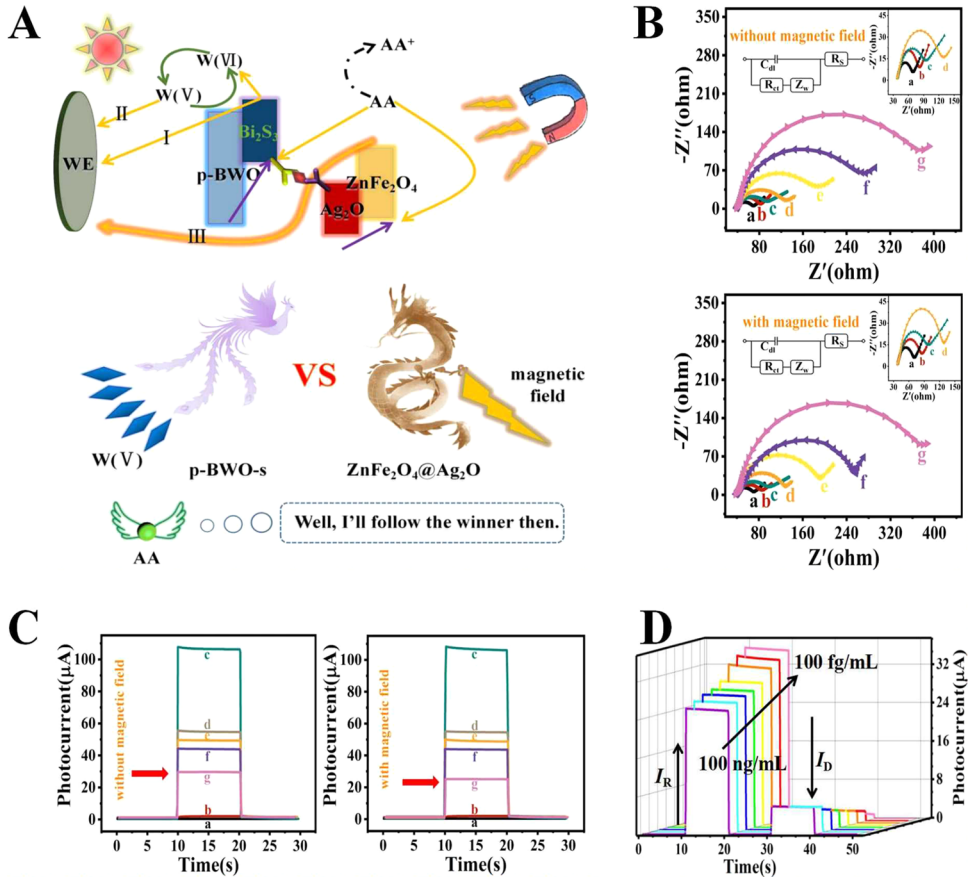

Figure 3. (A) Possible mechanism of the microfluidic ratiometric M-PEC biosensor for detecting NSE. Nyquist plots (B) and photocurrent response (C) (a) ITO, (b) p-BWO/ITO, (c) p-BWO-s/ITO, (d) Ab_1/p-BWO-s/ITO, (e) BSA/Ab_1/p-BWO-s/ITO, (f) NSE/BSA/Ab_1/p-BWO-s/ITO, and (g) Ab_2-$ZnFe_2O_4$@Ag_2O/NSE/BSA/Ab_1/p-BWO-s/ITO. (D) Photocurrent response of the microfluidic ratiometric M-PEC biosensor with different concentrations of NSE.

block the nonspecific active site. After washing, 10 μL of a certain concentration of the NSE antigen (from inlet 4) was injected. In addition, incubated, 10 μL of Ab_2-$ZnFe_2O_4$@Ag_2O (from inlet 5) was injected to fabricate the magnetic photoactive quenching label to incubate for 60 min at 37 °C. After each modification step, all washing procedures were performed using phosphate-buffered saline (PBS) (pH 7.0) to remove unabsorbed biomolecules. The biomolecules were injected at the inlet and flowed out through the outlet. All photocurrent responses were detected in the wavelength range of the stimulation resource LED. For more details, see the Supporting Information.

3. RESULTS AND DISCUSSION

3.1. Characterization of Photochromic Color Center-Mediated p-BWO-s nanosheets. X-ray diffraction (XRD) measurements were used to track the preparation procedure of p-BWO-s. As displayed in Figure S2, the pure p-BWO showed diffraction peaks corresponding to orthorhombic Bi_2WO_6 (JCPDS 73-2020). Except for the above characteristic peaks, several additional peaks were discovered in the p-BWO-s pattern, which were assigned to the lattice parameters of orthorhombic Bi_2S_3 (JCPDS 89-8963). Similar crystal structures promoted the formation and close contact of the p-BWO-s heterojunction. And scanning electron microscopy (SEM) images under different scales of p-BWO (Figure S3) and p-BWO-s (Figure S4) were shown for comparison. It could be seen from the figures that both p-BWO and p-BWO-s after vulcanization showed nanosheet structures, which were composed of abundant small nanoplates. The difference was that the p-BWO-s images showed a rougher surface due to the adsorption of Bi_2S_3. Further, the transmission electron microscopy (TEM) image of p-BWO-s is shown in Figure S5. The nanoparticles indicated that Bi_2S_3 was expectedly loaded. In addition, to further illustrate the successful preparation of p-BWO-s, the elemental distribution mapping (Figure 1) presented the Bi, W, O, Cl, and S elemental composition of p-BWO-s. And X-ray photoelectron spectroscopy (XPS) is used to characterize the surface chemical state of p-BWO-s as illustrated in Figure S6.

3.2. Characterization of Magnetic Photoactive $ZnFe_2O_4$@Ag_2O Nanospheres. XRD patterns of $ZnFe_2O_4$ and $ZnFe_2O_4$@Ag_2O are shown in Figure 2A. The peaks in the brown curve could be assigned to the cubic $ZnFe_2O_4$ phase (JCPDS 22-1012). In addition to the above characteristic peaks, there were also characteristic peaks in the gray curve, which could be matched to cubic Ag_2O (JCPDS 41-1104). The above results indicate that $ZnFe_2O_4$@Ag_2O was successfully prepared. The magnetization curves of $ZnFe_2O_4$ and $ZnFe_2O_4$@Ag_2O are shown in Figure 2B. The magnetization of $ZnFe_2O_4$@Ag_2O was lower than that of pure $ZnFe_2O_4$. Most notably, the magnetization curves of both showed obvious superparamagnetism.[28] Without the effect of remanence, superparamagnetism of $ZnFe_2O_4$@Ag_2O ensured reproducibility in the magnetic-resolved microfluidic ratio-

https://doi.org/10.1021/acs.analchem.1c03171
Anal. Chem. 2021, 93, 13680−13686

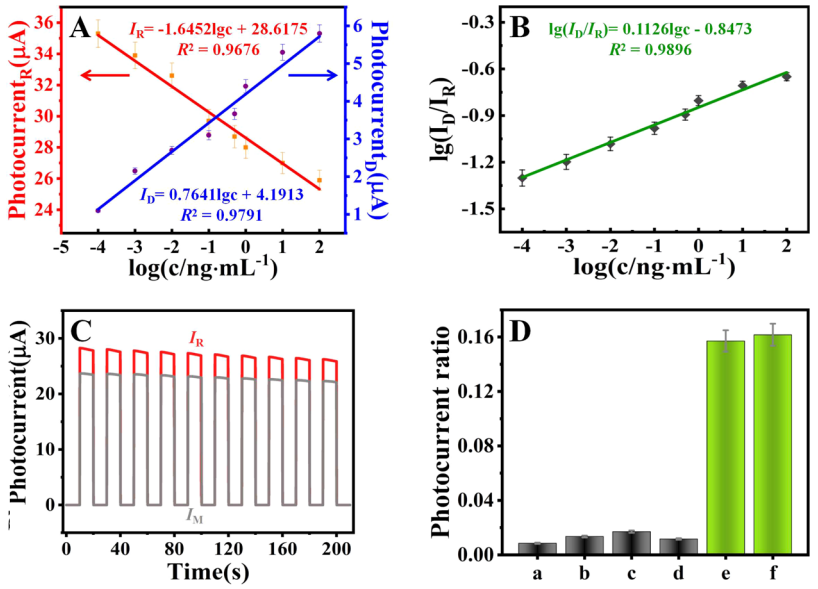

Figure 4. (A) Logarithmic standard curves between photocurrent I_R, I_D, and the concentration of NSE. (B) Logarithmic standard curve between ratiometric photocurrent and the concentration of NSE. (C) Stability assessment of I_R and I_D, *c*NSE = 0.1 ng/mL. (D) Specificity of the microfluidic ratiometric M-PEC biosensor for NSE detection over interferences: AFP (a), CEA (b), TPS (c), PSA (d), NSE (e), and mixture (f) (the concentrations of (a−d) were 10 ng/mL and that of (e) was 0.1 ng/mL).

metric PEC biosensor. In Figure 2C, the TEM image of $ZnFe_2O_4$@Ag_2O was displayed. The image revealed that reflected $ZnFe_2O_4$@Ag_2O was nanospheres composed of multiple single domain magnetic nanocrystals. In addition, Ag_2O was observed to be immobilized on the surface of $ZnFe_2O_4$ nanospheres (Figure 2D). Phase boundaries and two kinds of lattice fringes provided strong evidence for the formation of $ZnFe_2O_4$@Ag_2O heterojunction. In addition, the elemental distribution mapping presented the Zn, Fe, O, and Ag elemental composition of $ZnFe_2O_4$@Ag_2O (Figure S7). SEM images of $ZnFe_2O_4$ and $ZnFe_2O_4$@Ag_2O are shown in Figures S8 and S9, respectively. Interestingly, hollow structure was observed in both of them. The unique hollow structure could enhance the photoactivity of $ZnFe_2O_4$@Ag_2O.[29,30] Incidentally, the XPS and relevant discussion of $ZnFe_2O_4$@Ag_2O were recorded as in the Supporting Information.

3.3. Possible Working Mechanism of the Microfluidic Ratiometric M-PEC Biosensor. Under visible light irradiation, the possible working mechanism of the microfluidic ratiometric M-PEC biosensor is shown in Figure 3A. In short, by introducing an external magnetic field, the photoactivity of $ZnFe_2O_4$@Ag_2O is improved, which leads to a stronger competition between the $ZnFe_2O_4$@Ag_2O and the p-BWO-s platform for ascorbic acid (AA). Specifically, the orange curve in Figure 3A represents the electron transport path, and the purple curve represents the hole transport path. They are the main output channels of anode photocurrent.

For p-BWO-s platform, photogenerated electrons are transferred directly from Bi_2S_3 to the ITO glass surface via p-BWO along channel I due to the cascade band edge levels. At the same time, the color centers involving channel II further inhibit the recombination of electron−hole pairs (electron transfer direction: Bi_2S_3 → W (VI) → W (V) → W(VI) → ITO).[31] The existence of channel II is confirmed by comparing the photoactivity of p-BWO-s with the original Bi_2WO_6 after vulcanization (BWO-s) as shown in Figure S11. For the secondary antibody marker, $ZnFe_2O_4$@Ag_2O significantly reduces the photocurrent signal by the steric hindrance effect and competition with p-BWO-s for AA, just like channel III. Since the contribution photocurrent of channel III is much less than the lost photocurrent of channels I and II, the photocurrent signal is quenched. At this time, the measured routine photocurrent signal is defined as I_R. In the presence of an external magnetic field, the competitiveness of $ZnFe_2O_4$@Ag_2O (channel III) has been enhanced. At the same time, channels I and II are further weakened. As a result, photocurrent under an external magnetic field (I_M) decreases again on the basis of I_R. The difference photocurrent (I_D, namely I_R−I_M) increases with the increase of the concentration of NSE antigen. The enhancement of the photoactivity of $ZnFe_2O_4$@Ag_2O in the magnetic field is shown in Figure S12.

To further explore the change of $ZnFe_2O_4$@Ag_2O under a magnetic field, we tracked the layer-by-layer modification process of the biosensor. Nyquist plot measurements are characterized as shown in Figure 3B. The charge transfer resistance increased layer by layer, especially after binding to nonconducting biomolecules. Interestingly, the presence or absence of a magnetic field has little effect on the test results. Therefore, the negative magnetoresistance effect of $ZnFe_2O_4$@Ag_2O in the magnetic field is excluded. However, the photocurrent responses are different by controlling the magnetic field after connecting $ZnFe_2O_4$@Ag_2O (Figure 3C). Compared with the nearly constant photocurrent signals in other layers, this result proved the specific effect of the magnetic field on $ZnFe_2O_4$@Ag_2O rather than p-BWO-s and other biomolecules. Combined with previous work, the main reason for the photoactivity enhancement of $ZnFe_2O_4$@Ag_2O under the magnetic field may be electron spin polarization.[24] Under the magnetic field, more photogenerated electrons and holes are in the same spin state. This phenomenon is beneficial to the suppression of photogenerated electron−hole recombination.

3.4. Analytical Performance. To obtain the best analysis performance, optimal conditions were selected as shown in

https://doi.org/10.1021/acs.analchem.1c03171
Anal. Chem. 2021, 93, 13680−13686

Figure S13. Under optimal conditions, the response photocurrent of different concentrations of NSE antigen was measured in the absence and presence of an external magnetic field (Figure 3D). The photocurrent I_R decreased with the increase of NSE concentration. On the contrary, the photocurrent I_D increased gradually, which proved the feasibility of the microfluidic ratiometric M-PEC biosensor (from 100 fg/mL to 100 ng/mL). Figure 4A shows the linear relationship between the photocurrent and NSE antigen concentration. In Figure 4B, the ratiometric photocurrent of I_D/I_R shows a good linear relationship with NSE concentration. The linear regression equation was $\lg(I_D/I_R) = 0.1126 \lg c - 0.8473$ and the detection limit was 33 fg/mL (S/N = 3). Compared with other reported methods (Table S1) and other PEC biosensors (Table S2), the microfluidic ratiometric M-PEC biosensor constructed in this paper showed excellent performance. In addition, we explored the stability of the microfluidic ratiometric M-PEC biosensor. The photocurrent was relatively stable during 10 on−off cycles (Figure 4C). As shown in Figure 4D, the photocurrent signal in the presence of target NSE was significantly different from those of other individual interfering agents. The results showed good specificity of the microfluidic ratiometric M-PEC biosensor for the NSE antigen. Furthermore, we used the standard addition method to study the feasibility and accuracy of the microfluidic ratiometric M-PEC biosensor in the detection of human serum samples (see Table S3 for details). The recoveries of NSE were from 97.13 to 104.7% with relative standard deviations from 1.8 to 3.2%. These results indicated that the constructed microfluidic ratiometric M-PEC biosensor possessed great potential for the ultrasensitive, accurate, and practical determination of the NSE antigen.

4. CONCLUSIONS

In brief, a microfluidic ratiometric M-PEC biosensor was successfully developed. Based on the principle of magnetic resolution, the interference of environmental factors could be eliminated. Compared with the traditional PEC microfluidic biosensors, the highlights of this work could be summarized as follows: (1) the magnetic field could control the photoelectric response of photoactive materials; (2) the proposed microfluidic ratiometric M-PEC biosensor was not constrained by large-volume space-resolution equipment and wavelength-dependent or potential-dependent paired photoactive materials; (3) the photocurrent response of the platform was effectively enhanced by the color center defect; and (4) the proposed microfluidic ratiometric M-PEC biosensor could be extended to other biological analytes, even other biological analysis modes. In a proof-of-concept experiment, the biosensor was used for the detection of the NSE antigen and showed excellent sensitivity, selectivity, and stability. Importantly, the microfluidic ratiometric M-PEC biosensor opens up a new perspective development of PEC biosensor detection strategies.

■ ASSOCIATED CONTENT

Supporting Information

The Supporting Information is available free of charge at https://pubs.acs.org/doi/10.1021/acs.analchem.1c03171.

Materials, apparatuses, and test conditions; preparation of materials, microfluidic microelectrode, and microelectrode scheme; real photo of microelectrode; XRD patterns of p-BWO and p-BWO-s; SEM images of p-BWO and p-BWO-s; TEM image of p-BWO-s; XPS spectrum of p-BWO-s; elemental mapping image of $ZnFe_2O_4$@Ag_2O; SEM images of $ZnFe_2O_4$ and $ZnFe_2O_4$@Ag_2O; XPS spectrum of $ZnFe_2O_4$@Ag_2O; comparison of BWO-s and p-BWO-s photocurrent; comparison of $ZnFe_2O_4$@Ag_2O photocurrent with and without a magnetic field; optimization of experimental conditions; comparison of different methods for NSE; comparison of recent PEC biosensors for NSE; and testing of NSE in serum samples (PDF)

■ AUTHOR INFORMATION

Corresponding Authors

Jinhui Feng − *Collaborative Innovation Center for Green Chemical Manufacturing and Accurate Detection, Key Laboratory of Interfacial Reaction & Sensing Analysis in Universities of Shandong, University of Jinan, Jinan 250022, P. R. China*; Email: fengjinhui2011@163.com

Qin Wei − *Collaborative Innovation Center for Green Chemical Manufacturing and Accurate Detection, Key Laboratory of Interfacial Reaction & Sensing Analysis in Universities of Shandong, University of Jinan, Jinan 250022, P. R. China*; orcid.org/0000-0002-3034-8046; Email: sdjndxwq@163.com

Authors

Qian Cheng − *Collaborative Innovation Center for Green Chemical Manufacturing and Accurate Detection, Key Laboratory of Interfacial Reaction & Sensing Analysis in Universities of Shandong, University of Jinan, Jinan 250022, P. R. China*

Tingting Wu − *Collaborative Innovation Center for Green Chemical Manufacturing and Accurate Detection, Key Laboratory of Interfacial Reaction & Sensing Analysis in Universities of Shandong, University of Jinan, Jinan 250022, P. R. China*

Nuo Zhang − *Collaborative Innovation Center for Green Chemical Manufacturing and Accurate Detection, Key Laboratory of Interfacial Reaction & Sensing Analysis in Universities of Shandong, University of Jinan, Jinan 250022, P. R. China*

Xueying Wang − *Collaborative Innovation Center for Green Chemical Manufacturing and Accurate Detection, Key Laboratory of Interfacial Reaction & Sensing Analysis in Universities of Shandong, University of Jinan, Jinan 250022, P. R. China*

Hongmin Ma − *Collaborative Innovation Center for Green Chemical Manufacturing and Accurate Detection, Key Laboratory of Interfacial Reaction & Sensing Analysis in Universities of Shandong, University of Jinan, Jinan 250022, P. R. China*; orcid.org/0000-0002-7061-8944

Xu Sun − *Collaborative Innovation Center for Green Chemical Manufacturing and Accurate Detection, Key Laboratory of Interfacial Reaction & Sensing Analysis in Universities of Shandong, University of Jinan, Jinan 250022, P. R. China*; orcid.org/0000-0001-8762-4243

Complete contact information is available at: https://pubs.acs.org/10.1021/acs.analchem.1c03171

Notes

The authors declare no competing financial interest.

■ ACKNOWLEDGMENTS

This study was supported by the National Key Scientific Instrument and Equipment Development Project of China (No. 21627809), Q.W. thanks the Special Foundation for Taishan Scholar Professorship of Shandong Province, the Jinan Scientific Research Leader Workshop Project (2018GXRC024 and 2018GXRC021), the Innovation Team Project of Colleges and Universities in Jinan (No. 2019GXRC027), and the Natural Science Foundation of Shandong Province (ZR2020QB097).

■ REFERENCES

(1) Senel, M.; Dervisevic, E.; Alhassen, S.; Dervisevic, M.; Alachkar, A.; Cadarso, V. J.; Voelcker, N. H. *Anal. Chem.* **2020**, *92*, 12347−12355.
(2) Liao, Z.; Wang, J.; Zhang, P.; Zhang, Y.; Miao, Y.; Gao, S.; Deng, Y.; Geng, L. *Biosens. Bioelectron.* **2018**, *121*, 272−280.
(3) Szydzik, C.; Gavela, A. F.; Herranz, S.; Roccisano, J.; Knoerzer, M.; Thurgood, P.; Khoshmanesh, K.; Mitchell, A.; Lechuga, L. M. *Lab Chip* **2017**, *17*, 2793−2804.
(4) Yang, H.; Hu, M.; Li, Z.; Zhao, P.; Xie, L.; Song, X.; Yu, J. *Anal. Chem.* **2019**, *91*, 14577−14585.
(5) Zhou, Q.; Lin, Y.; Zhang, K.; Li, M.; Tang, D. *Biosens. Bioelectron.* **2018**, *101*, 146−152.
(6) Feng, J.; Dai, L.; Ren, X.; Ma, H.; Wang, X.; Fan, D.; Wei, Q.; Wu, R. *Anal. Chem.* **2021**, *93*, 7125−7132.
(7) Cao, J.-T.; Lv, J.-L.; Dong, Y.-X.; Liao, X.-J.; Ren, S.-W.; Liu, Y.-M. *J. Electroanal. Chem.* **2021**, *895*, No. 115468.
(8) Zhang, Y.; Hao, N.; Zhou, Z.; Hua, R.; Qian, J.; Liu, Q.; Li, H.; Wang, K. *Chem. Commun.* **2017**, *53*, 5810−5813.
(9) Zhu, C.; Liu, D.; Li, Y.; Shen, X.; Li, L.; Liu, Y.; You, T. *Curr. Opin. Electrochem.* **2019**, *17*, 47−55.
(10) Hu, C.; Tu, S.; Tian, N.; Ma, T.; Zhang, Y.; Huang, H. *Angew. Chem., Int. Ed.* **2021**, *60*, 16309−16328.
(11) Li, X.; Wang, W.; Dong, F.; Zhang, Z.; Han, L.; Luo, X.; Huang, J.; Feng, Z.; Chen, Z.; Jia, G.; Zhang, T. *ACS Catal.* **2021**, *11*, 4739−4769.
(12) Yu, F.; Wang, C.; Li, Y.; Ma, H.; Wang, R.; Liu, Y.; Suzuki, N.; Terashima, C.; Ohtani, B.; Ochiai, T.; Fujishima, A.; Zhang, X. *Adv. Sci.* **2020**, *7*, No. 2000204.
(13) Lu, Y.; Li, Y.; Wang, Y.; Zhang, J. *Appl. Catal., B* **2020**, *272*, No. 118979.
(14) Yang, M. Q.; Shen, L.; Lu, Y.; Chee, S. W.; Lu, X.; Chi, X.; Chen, Z.; Xu, Q. H.; Mirsaidov, U.; Ho, G. W. *Angew. Chem., Int. Ed.* **2019**, *58*, 3077−3081.
(15) Zhao, X.; Gao, W.; Liu, Q.; Cui, C.; Zhou, W.; Wang, X.; Zhang, X. L.; Zhao, L.; Sang, Y.; Liu, H. *Chem. Eng. J.* **2021**, *404*, No. 126972.
(16) Zhao, J.; Li, N.; Yu, R.; Zhao, Z.; Nan, J. *Chem. Eng. J.* **2018**, *349*, 530−538.
(17) Tang, R.; Zhou, S.; Li, C.; Chen, R.; Zhang, L.; Zhang, Z.; Yin, L. *Adv. Funct. Mater.* **2020**, *30*, No. 2000637.
(18) Feng, K.; Lin, Y.; Guo, J.; Ye, Z.; Zhang, Y.; Ma, Q.; Shao, Y.; Chen, K.; Zhuang, J.; Lin, D.; Lin, T. *J. Hazard. Mater.* **2020**, *393*, No. 122488.
(19) Zhou, J.; You, Z.; Xu, W.; Su, Z.; Qiu, Y.; Gao, L.; Yin, C.; Lan, L. *Sci. Rep.* **2019**, *9*, No. 5470.
(20) Zhou, X.; Yan, F.; Wu, S.; Shen, B.; Zeng, H.; Zhai, J. *Small* **2020**, *16*, No. 2001573.
(21) Singh, S.; Khare, N. *Nano Energy* **2017**, *42*, 173−180.
(22) Wang, Z.; Hu, T.; He, H.; Fu, Y.; Zhang, X.; Sun, J.; Xing, L.; Liu, B.; Zhang, Y.; Xue, X. *ACS Sustainable Chem. Eng.* **2018**, *6*, 10162−10172.
(23) Li, N.; Tu, Y.; Wang, K.; Huang, D.; Shen, Q.; Chen, W.; Zhou, J.; Ma, Q.; Liu, M. *Chem. Eng. J.* **2021**, *421*, No. 129940.
(24) Gao, W.; Peng, R.; Yang, Y.; Zhao, X.; Cui, C.; Su, X.; Qin, W.; Dai, Y.; Ma, Y.; Liu, H.; Sang, Y. *ACS Energy Lett.* **2021**, *6*, 2129−2137.
(25) Li, J.; Pei, Q.; Wang, R.; Zhou, Y.; Zhang, Z.; Cao, Q.; Wang, D.; Mi, W.; Du, Y. *ACS Nano* **2018**, *12*, 3351−3359.
(26) Bai, S.; Zhang, N.; Gao, C.; Xiong, Y. *Nano Energy* **2018**, *53*, 296−336.
(27) Maarisetty, D.; Baral, S. S. *J. Mater. Chem. A* **2020**, *8*, 18560−18604.
(28) Liu, J.; Zhang, Y.; Nan, Z. *Mater. Res. Bull.* **2014**, *60*, 270−278.
(29) Zhu, W.; Chen, Z.; Pan, Y.; Dai, R.; Wu, Y.; Zhuang, Z.; Wang, D.; Peng, Q.; Chen, C.; Li, Y. *Adv. Mater.* **2019**, *31*, No. 1800426.
(30) Xiao, M.; Wang, Z.; Lyu, M.; Luo, B.; Wang, S.; Liu, G.; Cheng, H. M.; Wang, L. *Adv. Mater.* **2019**, *31*, No. 1801369.
(31) Cao, X.; Chen, Z.; Lin, R.; Cheong, W.-C.; Liu, S.; Zhang, J.; Peng, Q.; Chen, C.; Han, T.; Tong, X.; Wang, Y.; Shen, R.; Zhu, W.; Wang, D.; Li, Y. *Nat. Catal.* **2018**, *1*, 704−710.

https://doi.org/10.1021/acs.analchem.1c03171
Anal. Chem. 2021, 93, 13680−13686